

DLA based compressed sensing for high resolution MR microscopy of neuronal tissue



Khieu-Van Nguyen^{a,b}, Jing-Rebecca Li^c, Guillaume Radecki^a, Luisa Ciobanu^{a,*}

^a Neurospin, CEA Saclay, 91191 Gif sur Yvette, France

^b University Paris-Sud, XI, 91450 Orsay, France

^c INRIA-Saclay, Equipe DEFI, CMAP, Ecole Polytechnique, 91128 Palaiseau, France

ARTICLE INFO

Article history:

Received 4 June 2015

Revised 14 August 2015

Available online 31 August 2015

Keywords:

Magnetic resonance imaging (MRI)

Compressed sensing (CS)

Magnetic resonance microscopy (MRM)

Cell segmentation

Diffusion limited aggregation (DLA)

Total variation (TV)

ABSTRACT

In this work we present the implementation of compressed sensing (CS) on a high field preclinical scanner (17.2 T) using an undersampling trajectory based on the diffusion limited aggregation (DLA) random growth model. When applied to a library of images this approach performs better than the traditional undersampling based on the polynomial probability density function. In addition, we show that the method is applicable to imaging live neuronal tissues, allowing significantly shorter acquisition times while maintaining the image quality necessary for identifying the majority of neurons via an automatic cell segmentation algorithm.

© 2015 Elsevier Inc. All rights reserved.

1. Introduction

Despite the fact that the modern magnetic resonance imaging (MRI) hardware available today often results in sufficiently high signal-to-noise ratio (SNR) without signal averaging, the total experimental time, dictated only by the requirement for sufficient k-space coverage, can be extremely long, prohibiting the very high resolution imaging of live biological systems. One way to reduce the data acquisition time is by undersampling the k-space, a strategy proposed by several methods including parallel imaging and compressed sensing. When the k-space is undersampled Fourier reconstructions produce aliasing artifacts. Non-uniform undersampling strategies can reduce these artifacts but often with a loss in image signal to noise ratio [1–5]. Parallel imaging exploits redundancy in k-space reconstructing the image from data acquired simultaneously with an array of radio frequency coils [6,7]. Using the latest developments in wire bonding technology phase array microcoils have been recently reported [8,9]. However, the small sample size renders the construction of such micro-arrays difficult and limits the applicability of parallel imaging to high resolution MR microscopy. Compressed sensing (CS) is a novel signal processing technique introduced by Donoho in 2006 [10]. The use of CS methods in the acquisition and reconstruction of magnetic

resonance images has been reported for cardiac imaging [11–14], hyper-polarized spectroscopic imaging [15] and more recently, diffusion tensor imaging [16] and MRI velocimetry [17].

CS produces images from significantly fewer data points than what is required by the Nyquist criterion using a non-linear reconstruction which enforces both sparsity of the image representation and consistency with the acquired data. The main requirement for undersampled k-space CS data is incoherence. Starting from this and considering the MR hardware constrains several ways of generating undersampling patterns have been proposed. The most commonly used undersampling schemes, either Cartesian or non-Cartesian, consist of variable-density random trajectories [11] based on a probability density function. Here we introduce a new method to generate undersampling patterns based on the diffusion limited aggregation (DLA) random growth model [18]. The implementation of the method requires minimum pulse sequence modifications as it undersamples the phase encoding dimensions of a standard 3D fast spin echo acquisition (rapid acquisition with relaxation enhancement (RARE)). The new acquisition scheme (CS-RARE) reduces the experimental time by a factor of two (50%) while preserving the signal to noise ratio, spatial resolution and image contrast. The undersampled data is reconstructed using a 3D extension of the Sparse MRI toolbox [11] with a total-variation (TV) penalty. CS-RARE image quality is assessed by comparing fully encoded and undersampled images of water phantoms and biological tissues. An automatic cell segmentation algorithm

* Corresponding author.

E-mail address: luisa.ciobanu@cea.fr (L. Ciobanu).

applied to 3D images of buccal and abdominal ganglia of *Aplysia californica* (25 μm isotropic resolution) allows us to further evaluate the performance of the CS-RARE acquisition. We find that DLA based compressed sensing is applicable to imaging live neuronal tissues, allowing significantly shorter acquisition times while providing the image quality necessary for identifying the majority of neurons.

2. Methods

2.1. Undersampling pattern

CS undersampling patterns are subsets of frequency domain points which are incoherent with respect to the sparsifying transform and satisfy hardware constraints. The most commonly used CS designs are obtained by generating quasi-random patterns following a Monte Carlo procedure based on a variable probability density function [11,19,20]. Here, we propose a new way of producing undersampling patterns employing the DLA random growth model.

DLA was proposed, for the first time, by Witten and Sander in 1981 [18]. The basic DLA process consists in the following steps:

1. An initial particle, the seed, is placed at the origin of a 2-dimensional lattice containing $M \times N$ points.
2. A kill circle, whose radius is much larger than the linear size of the lattice and centered on the seed, is defined.
3. A walker is launched at a random position on a birth circle with radius R_i defined by:

$$R_i = \frac{1}{100} \times \max(M, N) \times \left(1 + 49 \times \frac{i-1}{P}\right), \quad (1)$$

with $i = 1$ to P , where P is the desired final number of particles in the cluster, dictated by the undersampling ratio. If the radius of the birth circle is smaller than a predefined R_{min} (here we chose $R_{min} = 2$) then $R_i = R_{min}$.

4. The walker undergoes Brownian motion until one of three outcomes is reached:
 - (a) The walker escapes the kill circle. A new walker is placed on the same birth circle and the Brownian motion is restarted.
 - (b) The walker hits a lattice point which is a nearest neighbor to one member of the cluster. The walker then becomes part of the cluster and the index i is incremented to $i + 1$.
 - (c) The walker diffuses a long time without neither joining the cluster nor leaving the kill circle. The index i is incremented to $i + 1$, and there will be no contribution to the cluster from this walker. NOTE: If i reaches P while the number of particles in the cluster is smaller than P , the counter is reset to $i = 1$ (i.e. restart from the smallest birth circle).
5. Steps 3 and 4 are repeated until the desired cluster size is reached.

In our case the 2D lattices sampled belong to a 3D Cartesian k-space grid, predefined for a given field-of-view ($10 \times 2.2 \times 2.2 \text{ mm}^3$) and spatial resolution (25 μm isotropic), with the undersampling being done along the two phase encoding directions. Fig. 1a shows the proposed undersampling for one phase encoding plane. Such undersampling can be applied to a RARE acquisition with an acceleration factor $A_F = 4$ by generating independent subsampling patterns for k-space subsets corresponding to different echo times, resulting therefore in repeating the pattern in Fig. 1a four times (Fig. 1b). The 2D patterns obtained are repeated for each point in the read direction to generate the 3D undersampling pattern (Fig. 1c). Eleven undersampling ratios were chosen between 20% and 70%. For each undersampling ratio 300 sets consisting of

100 undersampling masks were generated and from each set the mask with the lowest Point Spread Function (PSF) was selected [11]. The 3300 masks produced were then applied to a library of a priori acquired fully sampled data sets consisting of six images of abdominal and buccal ganglia of *Aplysia californica* (three of each). Undersampling patterns based on the polynomial probability density function, extended to a 3D RARE acquisition with $A_F = 4$ (Fig. 1d), were also generated as in [11] and were applied to the same library of images. In order to compare the two undersampling strategies we computed the relative errors (RE) between the CS and fully encoded images:

$$RE = \frac{\sqrt{\sum_{i=1}^n (y_i - \hat{y}_i)^2}}{\sqrt{\sum_{i=1}^n y_i^2}}, \quad (2)$$

where y_i and \hat{y}_i are the signal intensities corresponding to voxel i in the fully encoded image and the undersampled image, respectively. In addition, the performances of DLA and polynomial schemes when applied to RARE acquisitions with $A_F = 1$ were similarly evaluated this time applying the generated masks to a fully encoded image of the buccal ganglia acquired without acceleration.

The DLA sampling pattern with the minimum relative error was implemented in Paravision 5.0 (Bruker BioSpin, Ettlingen, Germany) by modifying the existent RARE pulse sequence.

2.2. Sample preparation and data acquisition

All experiments were performed at 19 °C on a 17.2 T system (Bruker BioSpin, Ettlingen, Germany) equipped with 1 T/m gradients. RF transceivers were home-built microcoils with inner diameters of 2.4 mm, the design of which has been described elsewhere [21,22]. Typically, two acquisitions were acquired for each sample. A standard, fully encoded RARE acquisition with a matrix size of $400 \times 88 \times 88$ and a CS undersampling RARE acquisition (CS-RARE) with a matrix size reduced to 50%. All the other parameters were identical for the two acquisitions: TR = 3500 ms, TE = 20 ms, RARE $A_F = 4$, FOV = $10 \times 2.2 \times 2.2 \text{ mm}^3$. One fully encoded image of the buccal ganglia was acquired without acceleration.

Phantom samples: SNR measurements were performed on images obtained using CS and fully encoded RARE acquisitions on phantom samples. The latter were 2 mm ID glass capillaries (Vitro-Com, Mountain Lakes, NJ, USA) filled with artificial sea water (ASW) (NaCl, 450 mM; KCl, 10 mM; MgCl₂, 30 mM; MgSO₄, 20 mM). All chemicals were purchased from Sigma–Aldrich (Saint Luis, MO, USA).

Neuronal tissue: Five *Aplysia californica* (National Resource for Aplysia, Miami, FL, USA) were used in this study. Four animals were used for generating the libraries necessary to optimize the undersampling trajectories, and one was used to acquire both fully encoded and CS DLA undersampled images. The animals were anaesthetized by injection of an isotonic magnesium chloride solution (MgCl₂, 360 mM; HEPES, 10 mM; pH 7.5). The buccal and abdominal ganglia were resected and inserted into a 2.0 mm ID glass capillary filled with ASW and then slid inside the transceiver for imaging.

2.3. Image reconstruction

The fully encoded images were processed directly in Paravision. For the reconstruction of CS undersampled data we followed the algorithm provided by Lustig et al. in the SparseMRI toolbox [11], which we extended to a 3D version. Briefly, if we denote the undersampled Fourier transform corresponding to the k-space undersampled pattern \mathcal{F} , and \mathcal{W} the Wavelet transform, the

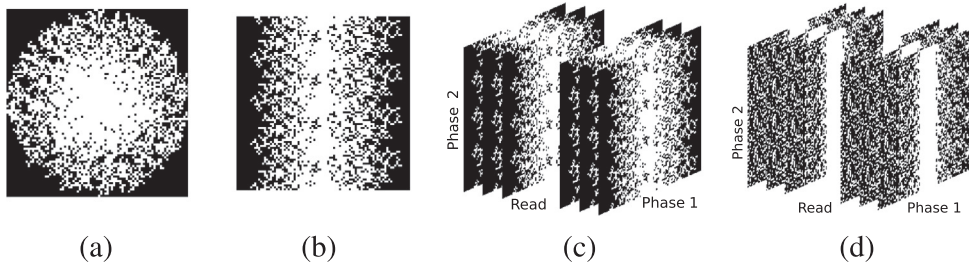


Fig. 1. Undersampling patterns (50%) for a RARE acquisition. (a) DLA undersampled phase encoding plane for $A_r = 1$. (b) DLA undersampled phase encoding plane for $A_r = 4$. The DLA undersampling was applied for each group of k-space points corresponding to the same echo time, therefore 4 times. (c) 3D DLA undersampling. (d) 3D polynomial undersampling.

reconstructed image m is obtained by solving the following constrained optimization problem with total variation (TV) term:

$$\begin{aligned} & \text{minimize} \quad \|\mathcal{W}m\|_1 + \alpha TV(m), \\ & \text{s.t.} \quad \|\mathcal{F}m - y\|_2 < \epsilon, \end{aligned} \quad (3)$$

where α trades \mathcal{W} sparsity with finite differences sparsity, and y is the measured undersampled k-space data. The thresholding parameter ϵ is the expected noise level. The norms, \mathcal{L}_1 and \mathcal{L}_2 , are defined as $\|x\|_1 = \sum_i |x_i|$ and $\|x\|_2 = \sqrt{\sum_i |x_i|^2}$, respectively. Eq. (3) can be rewritten in the unconstrained problem form as following:

$$\arg \min_m \|\mathcal{F}m - y\|_2^2 + \lambda_1 \|\mathcal{W}m\|_1 + \lambda_2 TV(m), \quad (4)$$

where λ_1, λ_2 are two regularization constants. A large λ_2 tends to suppress image gradients and make the reconstructed image smooth, losing point-like features [23]. The main steps of this reconstruction algorithm are schematically represented in Fig. 2.

2.4. Cell segmentation

In this section we introduce a simple algorithm for automatic cell segmentation on MR T_2 weighted images. The main steps are as follows:

1. Different signal intensity levels ($C1, C2, C3$, etc.) contour maps are created from a given image data, $C0$.
2. The area for each contour map is computed and maps with areas larger than a predefined maximum are removed. This step removes the water region around the ganglia and the inner part of the ganglia not containing cells.
3. The contour maps are then thresholded several times in order to separate isolated cells or cell clusters. The thresholding stops when repeating the algorithm will lead to unwanted cell elimination.
4. The cells within the clusters are further separated (Fig. 3):
 - (a) 1s are assigned to pixels corresponding to cell regions and 0s to all the others. The 1s located on the cluster boundary are removed. (One pixel is considered as part of the boundary if connected with at least two 0 pixels.)
 - (b) 1s and 0s are inverted.

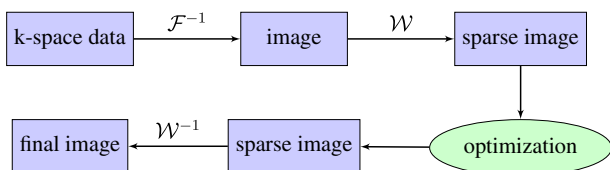


Fig. 2. Image reconstruction diagram: \mathcal{F}^{-1} is the inverse Fourier transform, \mathcal{W} and \mathcal{W}^{-1} are Wavelet and inverse Wavelet transforms, respectively.

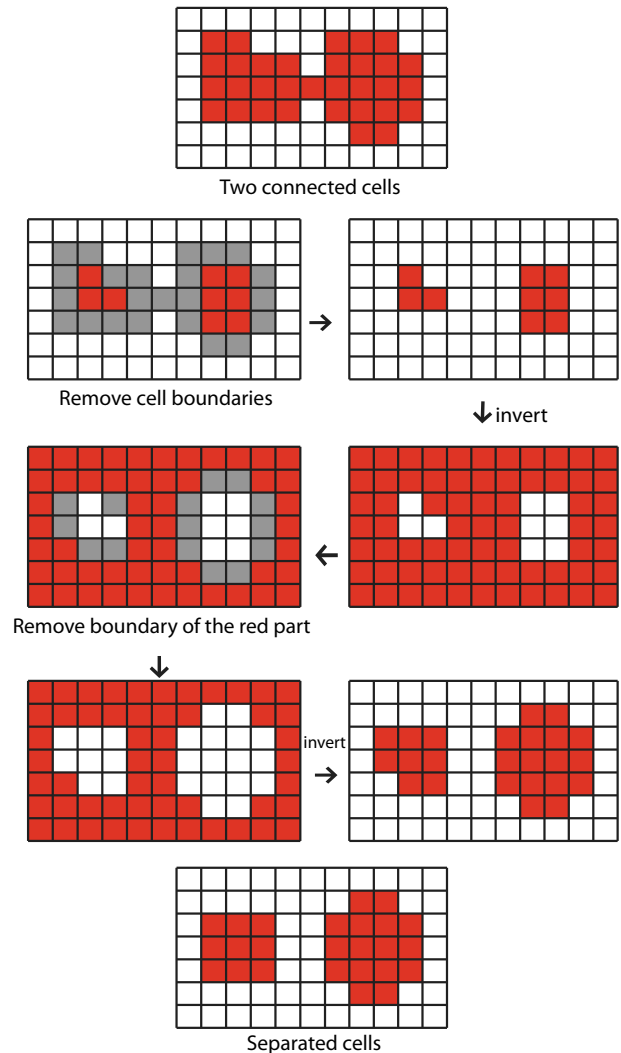


Fig. 3. Flow diagram illustrating the proposed algorithm for separating cells within clusters.

- (c) The boundary pixels are removed again.
- (d) The 1s and 0s are inverted.
- (e) Steps 4a–4d are repeated two or three times.
5. The cells detected in all the contour maps are combined. To avoid false detection one cell is considered “true” if it is detected in at least two maps.

The DLA undersampling pattern generation, the image reconstruction, and the cell segmentation algorithm were implemented in Matlab (MathWorks, Natick, MA, United States).

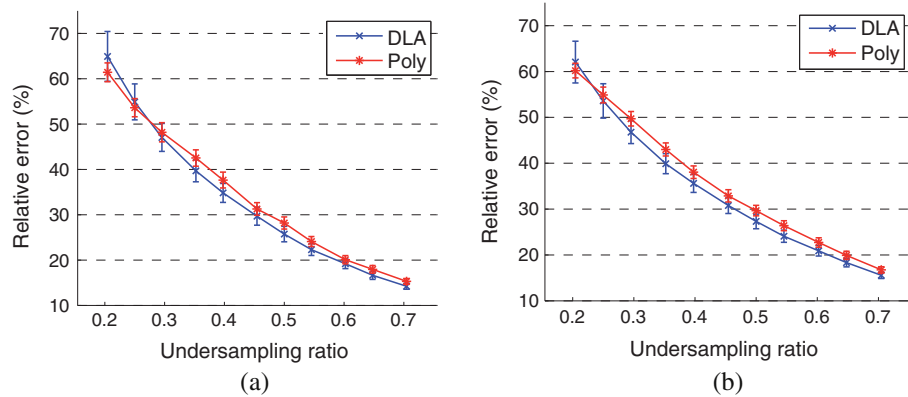


Fig. 4. The relative errors between the fully encoded and CS images obtained by applying DLA and polynomial undersampling schemes to abdominal (a) and buccal ganglia (b) image libraries as a function of the undersampling ratio. The fully encoded images were acquired using a standard RARE acquisition with $A_F = 4$. The error bars represent standard deviations ($n = 300$).

3. Results

3.1. Undersampling pattern

As seen in Fig. 4, in the case of RARE acquisitions with $A_F = 4$, for undersampling ratios superior to 0.25, the mean relative errors between the CS and the fully encoded images are smaller for DLA than for polynomial patterns for both the buccal and the abdominal ganglia. Moreover, the DLA method is more stable as the standard deviation of the relative error is smaller than for the

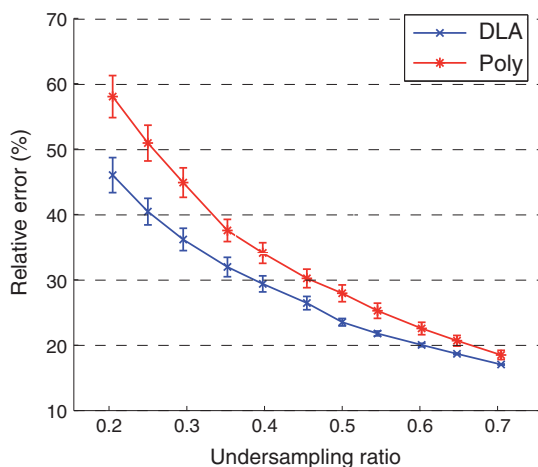


Fig. 5. The relative errors between the fully encoded and CS images obtained by applying DLA and polynomial undersampling schemes to a fully encoded (RARE acquisition with $A_F = 1$) image of buccal ganglia. The error bars represent standard deviations ($n = 300$).

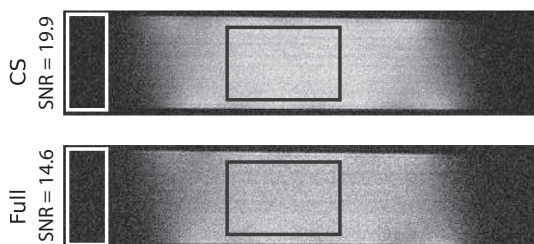


Fig. 6. CS (top) and fully encoded (bottom) images of a water phantom. The SNR was calculated as the mean of signal intensity (black ROI) divided by the standard deviation of the noise (white ROI).

polynomial scheme. In this study we used an undersampling ratio of 50% which corresponds to relative errors of 27% and 26% for the buccal and abdominal ganglia, respectively. For RARE acquisitions with $A_F = 1$ the difference in performance between the two undersampling schemes is even larger, as shown in Fig. 5.

3.2. Signal to noise ratio and spatial resolution

The reconstructed MR image of an ASW phantom acquired with the newly modified CS-RARE sequence was compared to the fully sampled MR image acquired with the conventional RARE sequence (Fig. 6). The signal to noise ratios obtained, calculated by dividing the mean signal value from a water region to the standard deviation of the noise in an ROI outside the sample, were found 19.9 and 14.6 for the CS and fully encoded data sets, respectively. The CS data set presents higher SNR than the fully encoded acquisition due to the reduction of noise in the CS reconstructed image. Specifically, the standard deviation of the noise (measured in the white ROI in Fig. 6) was found to be 165 and 120, respectively, for the two data sets, while the mean signal levels were similar (~ 2400).

To test the effect of CS undersampling on the spatial resolution we compared fully encoded and undersampled images of buccal and abdominal ganglia. For this particular comparison the undersampling was performed starting from the same fully sampled data set in order to avoid possible confounding factors such as coil instability or sample deterioration. Signal intensity profiles drawn across the sample (Fig. 7) demonstrate that no spatial or intensity information is lost. This was further confirmed by the Pearson correlation coefficients [24] between the fully and CS encoded images, calculated within a region containing the ganglia and consisting of approximately 180 000 voxels, which were found to be 0.90 and 0.91 for the buccal and abdominal samples, respectively.

To complete the CS performance assessment the automatic cell segmentation algorithm described in the Methods section was applied in each slice of the 3D fully encoded and CS images. The segmentation produced similar results for CS and fully encoded images, with an identical number of cells detected for abdominal ganglia and one false positive for the CS image (out of 31 cells) of the buccal ganglia (Fig. 8).

4. Conclusion and discussion

In this work we introduce a new way of generating CS undersampling trajectories based on the DLA algorithm and apply it to the undersampling of a RARE encoding acquisition scheme. Our results demonstrate that the DLA approach performs better than

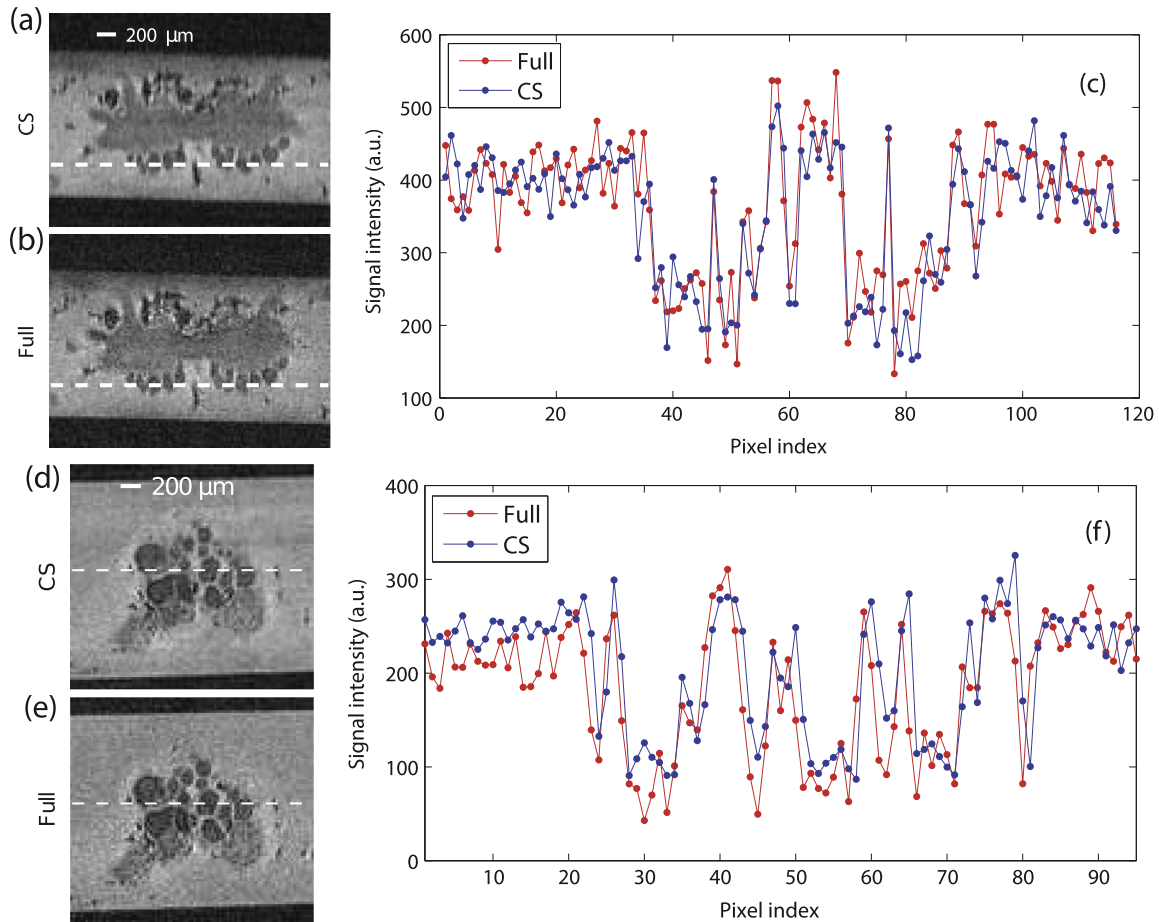


Fig. 7. Buccal (a, b) and abdominal (d, e) ganglia images acquired with a CS-RARE (a, d) and a standard RARE sequence (b, e), along with the signal intensity profiles (c, f) at locations indicated by the white lines across the images. The hypointense regions seen in the images correspond to cell bodies.

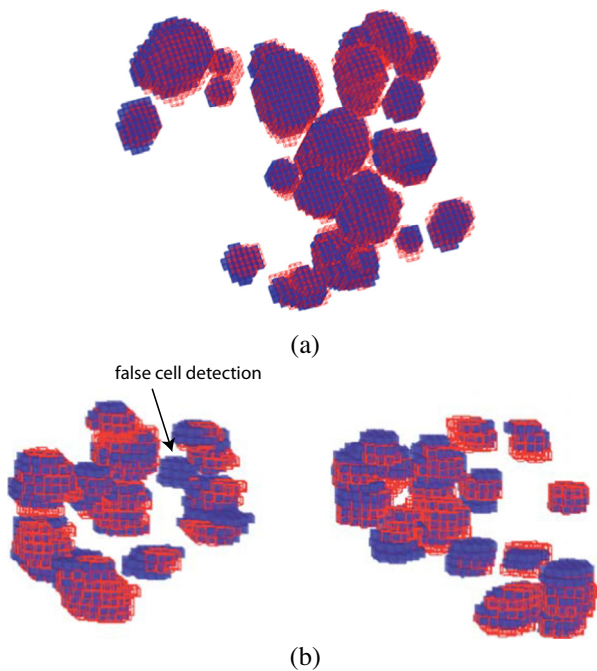


Fig. 8. Comparison between the cells detected on the fully encoded (red wire-frame) and CS (solid blue) images of abdominal (a) and buccal ganglia (b). An identical number of cells was detected on the abdominal ganglion with both acquisitions, while on the buccal ganglia one false positive was detected on the CS data set.

the standard polynomial strategy for undersamplings superior to 25% for acquisitions already accelerated ($A_F = 4$). In addition, we show that when used to image live neuronal tissue the proposed CS-RARE strategy maintains the spatial resolution and contrast to noise ratio necessary to the identification of the majority of neurons within *Aplysia* ganglia while reducing the acquisition time to 50%. While in the current implementation the DLA undersampling was applied to a RARE acquisition with an acceleration factor 4, the implementation to acquisitions with different acceleration factors is straightforward. As demonstrated here, the DLA approach performs significantly better for RARE acquisitions without acceleration, being therefore favorable for imaging species with short T_2 relaxation times. Moreover, the DLA undersampling is not limited to RARE acquisitions and can be easily extended to other types of sequences.

In conclusion, the results presented here suggest that DLA is a promising alternative to the standard polynomial CS undersampling strategy and may be beneficial to magnetic resonance microscopy studies by reducing the notoriously long acquisitions to more reasonable times, thus enabling the expansion of the technique to the study of living specimens and eventually to dynamic investigations.

Acknowledgment

This work was funded by grant ANR-13-BSV5-0014-01 (project ANImE) and by the doctoral school STITS, University Paris Sud, XI, 91405 Orsay, France. L. Ciobanu acknowledges Dr. Alexandre Vignaud for useful discussions.

References

- [1] G. Marseille, R. de Beer, M. Fuderer, A. Mehlkopf, D. van Ormondt, Nonuniform phase-encode distributions for MRI scan time reduction, *J. Magn. Reson. Ser. B* 111 (1) (1996) 70–75.
- [2] K. Scheffler, J. Hennig, Reduced circular field-of-view imaging, *Magn. Reson. Med.* 40 (3) (1998) 474–480.
- [3] C.-M. Tsai, D.G. Nishimura, Reduced aliasing artifacts using variable-density k-space sampling trajectories, *Magn. Reson. Med.* 43 (3) (2000) 452–458.
- [4] D.C. Peters, F.R. Korosec, T.M. Grist, W.F. Block, J.E. Holden, K.K. Vigen, C.A. Mistretta, Undersampled projection reconstruction applied to MR angiography, *Magn. Reson. Med.* 43 (1) (2000) 91–101.
- [5] A. Greiser, M. von Kienlin, Efficient k-space sampling by density-weighted phase-encoding, *Magn. Reson. Med.* 50 (6) (2003) 1266–1275.
- [6] M.A. Griswold, P.M. Jakob, R.M. Heidemann, M. Nittka, V. Jellus, J. Wang, B. Kiefer, A. Haase, Generalized autocalibrating partially parallel acquisitions (GRAPPA), *Magn. Reson. Med.* 47 (6) (2002) 1202–1210.
- [7] K.P. Pruessmann, M. Weiger, M.B. Scheidegger, P. Boesiger, SENSE: sensitivity encoding for fast MRI, *Magn. Reson. Med.* 42 (5) (1999) 952–962.
- [8] O.G. Gruschke, N. Baxan, L. Clad, K. Kratt, D. von Elverfeldt, A. Peter, J. Hennig, V. Badilita, U. Wallrabe, J.G. Korvink, Lab on a chip phased-array MR multi-platform analysis system, *Lab Chip* 12 (2012) 495–502.
- [9] K. Gbel, O.G. Gruschke, J. Leupold, J.S. Kern, C. Has, L. BrucknerTuderman, J. Hennig, D. von Elverfeldt, N. Baxan, J.G. Korvink, Phased-array of microcoils allows MR microscopy of ex vivo human skin samples at 9.4 T, *Skin Res. Technol.* 21 (1) (2015) 61–68.
- [10] D. Donoho, Compressed sensing, *IEEE Trans. Inf. Theory* 52 (4) (2006) 1289–1306.
- [11] M. Lustig, D. Donoho, J.M. Pauly, Sparse MRI: the application of compressed sensing for rapid MR imaging, *Magn. Reson. Med.* 58 (6) (2007) 1182–1195.
- [12] T. Wech, A. Lemke, D. Medway, L.-A. Stork, C.A. Lygate, S. Neubauer, H. Kostler, J. E. Schneider, Accelerating cine-MR imaging in mouse hearts using compressed sensing, *J. Magn. Reson. Imaging* 34 (5) (2011) 1072–1079.
- [13] T. Wech, D. Medway, C. Lygate, S. Neubauer, H. Kostler, J. Schneider, Accurate infarct-size measurements from accelerated, compressed sensing reconstructed cine-MRI images in mouse hearts, *J. Cardiovasc. Magn. Reson.* 14 (Suppl. 1) (2012) P57.
- [14] T. Wech, C. Lygate, S. Neubauer, H. Kostler, J. Schneider, Highly accelerated cardiac functional MRI in rodent hearts using compressed sensing and parallel imaging at 9.4 T, *J. Cardiovasc. Magn. Reson.* 14 (Suppl. 1) (2012) P65.
- [15] S. Hu, M. Lustig, A. Balakrishnan, P.E.Z. Larson, R. Bok, J. Kurhanewicz, S.J. Nelson, A. Goga, J.M. Pauly, D.B. Vigneron, 3D compressed sensing for highly accelerated hyperpolarized ¹³C MRSI with in vivo applications to transgenic mouse models of cancer, *Magn. Reson. Med.* 63 (2) (2010) 312–321.
- [16] Y. Wu, Y.-J. Zhu, Q.-Y. Tang, C. Zou, W. Liu, R.-B. Dai, X. Liu, E.X. Wu, L. Ying, D. Liang, Accelerated MR diffusion tensor imaging using distributed compressed sensing, *Magn. Reson. Med.* 71 (2) (2014) 763–772.
- [17] J. Paulsen, V.S. Bajaj, A. Pines, Compressed sensing of remotely detected MRI velocimetry in microfluidics, *J. Magn. Reson.* 205 (2) (2010) 196–201.
- [18] T.A. Witten, L.M. Sander, Diffusion-limited aggregation, a kinetic critical phenomenon, *Phys. Rev. Lett.* 47 (1981) 1400–1403.
- [19] P. Montesinos, J.F.P. Abascal, L. Cuss, J.J. Vaquero, M. Desco, Application of the compressed sensing technique to self-gated cardiac cine sequences in small animals, *Magn. Reson. Med.* 72 (2) (2014) 369–380.
- [20] P. Montesinos, J. Abascal, C. Chavarras, J. Vaquero, M. Desco, Compressed sensing for cardiac MRI cine sequences: a real implementation on a small-animal scanner, in: L.M. Roa Romero (Ed.), XIII Mediterranean Conference on Medical and Biological Engineering and Computing 2013, IFMBE Proceedings, vol. 41, Springer International Publishing, 2014, pp. 214–217.
- [21] I.O. Jelescu, R. Nargeot, D.L. Bihan, L. Ciobanu, Highlighting manganese dynamics in the nervous system of aplysia californica using MEMRI at ultra-high field, *NeuroImage* 76 (0) (2013) 264–271.
- [22] G. Radecki, R. Nargeot, I.O. Jelescu, D. Le Bihan, L. Ciobanu, Functional magnetic resonance microscopy at single-cell resolution in *Aplysia californica*, *Proc. Natl. Acad. Sci.* 111 (23) (2014) 8667–8672.
- [23] Z. Zhu, K. Wahid, P. Babyn, R. Yang, Compressed sensing-based MRI reconstruction using complex double-density dual-tree DWT, *J. Biomed. Imaging* 2013 (2013), 10:10–10:10.
- [24] A. Miranda Neto, A. Correa Victorino, I. Fantoni, D. Zampieri, J. Ferreira, D. Lima, Image processing using Pearson's correlation coefficient: applications on autonomous robotics, in: 13th International Conference on Autonomous Robot Systems (Robotica), 2013, pp. 1–6.